

A Si I atomic model for NLTE spectropolarimetric diagnostics of the 10827 Å line

N. G. Shchukina^{1,2}, A. V. Sukhorukov^{2,3}, and J. Trujillo Bueno^{1,4,5}

¹ Instituto de Astrofísica de Canarias, 38205 La Laguna, Tenerife, Spain

² Main Astronomical Observatory, National Academy of Sciences, 27 Zabolotnogo Street, 03143 Kiev, Ukraine

³ Institute for Solar Physics, Department of Astronomy, Stockholm University, AlbaNova University Centre, 106 91 Stockholm, Sweden

⁴ Departamento de Astrofísica, Universidad de La Laguna, 38206 La Laguna, Tenerife, Spain

⁵ Consejo Superior de Investigaciones Científicas, 28006 Madrid, Spain
e-mail: shchukin@mao.kiev.ua

Received 13 December 2016 / Accepted 14 March 2017

ABSTRACT

Aims. The Si I 10 827 Å line is commonly used for spectropolarimetric diagnostics of the solar atmosphere. First, we aim at quantifying the sensitivity of the Stokes profiles of this line to non-local thermodynamic equilibrium (NLTE) effects. Second, we aim at facilitating NLTE diagnostics of the Si I 10 827 Å line. To this end, we propose the use of a relatively simple silicon model atom, which allows a fast and accurate computation of Stokes profiles. The NLTE Stokes profiles calculated using this simple model atom are very similar to those obtained via the use of a very comprehensive silicon model atom.

Methods. We investigate the impact of the NLTE effects on the Si I 10 827 Å line by means of multilevel radiative transfer calculations in a three-dimensional (3D) model atmosphere taken from a state-of-the-art magneto-convection simulation with small-scale dynamo action. We calculate the emergent Stokes profiles for this line at the solar disk center and for every vertical column of the 3D snapshot model, neglecting the effects of horizontal radiative transfer.

Results. We find significant departures from LTE in the Si I 10 827 Å line, not only in the intensity but also in the linearly and circularly polarized profiles. At wavelengths around 0.1 Å, where most of the Stokes Q , U , and V peaks of the Si I 10 827 Å line occur, the differences between the NLTE and LTE profiles are comparable with the Stokes amplitudes themselves. The deviations from LTE increase with increasing Stokes Q , U , and V signals. Concerning the Stokes V profiles, the NLTE effects correlate with the magnetic field strength in the layers where such circular polarization signals are formed.

Conclusions. The NLTE effects should be taken into account when diagnosing the emergent Stokes I profiles as well as the Stokes Q , U , and V profiles of the Si I 10 827 Å line. The sixteen-level silicon model atom proposed here, with six radiative bound-bound transitions, is suitable to account for the physics of formation of the Si I 10 827 Å line and for modeling and inverting its Stokes profiles without assuming LTE.

Key words. magnetohydrodynamics (MHD) – Sun: photosphere – line: formation – radiative transfer – convection – dynamo

1. Introduction

The spectral region around 10 830 Å is a powerful diagnostic window to explore the physical properties of the solar atmosphere. It contains the He I 10 830 Å triplet and the Si I 10 827 Å line. While the helium triplet encodes information on chromospheric structures, the core of the silicon line originates in the upper photosphere, near the temperature minimum region of standard semi-empirical models. Both lines have sufficiently large effective Landé factors g_{eff} ; the Si I 10 827 Å line has $g_{\text{eff}} = 1.5$ and the He I triplet lines at 10 828.9, 10 830.3, and 10 830.3 Å lines have $g_{\text{eff}} = 2.0$, 1.75, and 0.875, respectively. Since they are located in the near infrared (IR) spectral region, the polarization signals induced by the Zeeman effect in these lines are more sensitive to the presence of a magnetic field than other lines in the optical part of the solar spectrum with similar or even larger g_{eff} values (see, e.g., Landi Degl'Innocenti & Landolfi 2004). For this reason, the Si I 10 827 Å line and the He I triplet are potentially useful for performing simultaneous diagnostics of magnetic fields in the photosphere and the chromosphere.

Lagg (2007), Trujillo Bueno (2010) and Penn (2014) review spectropolarimetric investigations of solar magnetic fields using the 10 830 Å spectral region. For example, full Stokes inversions of the Si I 10 827 Å line and the He I 10 830 Å triplet have been used to study the pre-flare, flare, and post-flare stages (Kuckein et al. 2015), active region filaments (Kuckein et al. 2012; Xu et al. 2012; Yelles et al. 2012), and complex active regions (Solanki et al. 2003; Wiegmann et al. 2005), as well as eruptions (Penn & Kuhn 1995).

The Si I 10 827 Å line and the He I 10 830 Å triplet have been used also to study waves in the solar atmosphere. In particular, Centeno et al. (2006, 2009) investigated the propagation of waves from the photosphere to the chromosphere in a sunspot umbra, as well as in a pore and a facula. Bloomfield et al. (2007) studied running penumbral waves in a sunspot and surrounding regions. Felipe et al. (2010, 2011a,b) used observations in these lines to simulate shock wave propagation in sunspots. Other applications of the Si I 10 827 Å line in solar physics include studies of long-term variations of the solar activity

(Livingston & Holweger 1982) and measurements of the solar differential rotation (Pierce & Lopresto 1984).

Scientific interest for the 10 830 Å spectral region has been growing over the last fifteen years following advances in theory as well as in IR instrumentation for spectropolarimetric observations. For example, the following facilities have been proposed, and some are presently under development: the 4-m Daniel K. Inouye Solar Telescope (DKIST, Keil et al. 2011), the 4-m European Solar Telescope (EST, Collados et al. 2013), the 1.5-m GREGOR solar telescope (Denker et al. 2012; Soltau et al. 2012), and the Japanese Aerospace Exploration Agency mission Solar-C (Shimizu et al. 2011; Katsukawa et al. 2012). The infrared instruments planned for DKIST will provide unprecedented IR observations on the solar disk, at the limb, and in the corona, with the highest possible spatial resolution from the ground. The GREGOR telescope hosts the GREGOR Infrared Spectrograph (GRIS, Collados et al. 2012), designed for spectropolarimetry in the 10 000–18 000 Å region.

Such unprecedented facilities for making solar IR spectropolarimetric observations require further development of diagnostic tools. Recent three-dimensional (3D) hydrodynamic (HD, see Asplund et al. 2009) and magnetohydrodynamic (MHD, see Stein 2012; Rempel 2014, and references therein) simulations have reached a high level of realism concerning the description of the solar photosphere. Inversion methods of spectral lines for which NLTE effects are significant (e.g., Socas-Navarro et al. 2015; Asensio Ramos et al. 2008) are being increasingly applied. Currently, the essential physics of formation of the Si I 10 827 Å line intensity (Stokes I parameter) is well known. In one-dimensional (1D) models of the solar atmosphere, such as MACKKL (Maltby et al. 1986), VAL-C (Vernazza et al. 1976, 1981), and HOLMUL (Holweger & Muller 1974), the NLTE intensity is lower than the LTE intensity in the core of this line (Bard & Carlsson 2008; Shi et al. 2008; Sukhorukov & Shchukina 2012). Significant departures from LTE in the Si I 10 827 Å line intensity have also been found in a 3D HD model atmosphere (Sukhorukov 2012). Nevertheless, the approximation of LTE is always used for inverting the Stokes parameters of this line, for example by applying the SIR code (Ruiz Cobo & del Toro Iniesta 1992).

In this paper, we investigate the magnitude of the deviations of the Stokes parameters I , Q , U , and V of the Si I 10 827 Å line from their LTE values. To this end, we study the silicon line formation problem in a 3D MHD model of the quiet solar photosphere taken from a magneto-convection simulation with small-scale dynamo action (Rempel 2014).

One of our aims is to develop the simplest possible model atom of Si I suitable for efficiently performing NLTE inversions of the Si I 10 827 Å line; obviously, the model atom must be sufficiently accurate to reproduce the NLTE Stokes profiles of the Si I 10 827 Å line calculated with a comprehensive atomic model. We note, that Bard & Carlsson (2008) already constructed a computationally tractable model of the Si I atom in order to study solar atmospheric dynamics using the Stokes- I profile of this line. Their model atom includes 23 levels and 171 radiative transitions. However, such an atomic model is still too complicated for performing NLTE inversions (e.g., with the NICOLE code of Socas-Navarro et al. 2015).

The paper is organized as follows. Section 2 describes the 3D snapshot model used in this study, the NLTE radiative transfer method used for the spectral synthesis of the Si I 10 827 Å line, and the silicon atomic models. Section 3 presents NLTE versus LTE results for the emergent Stokes profiles including the

departure coefficients of the atomic level populations, the line source function and the emergent Stokes I , Q , U , and V profiles. Finally, Section 4 summarizes our main conclusions.

2. Input data and method

2.1. Model atmosphere

We used a 3D snapshot model taken from the magnetoconvection simulations with small-scale dynamo (SSD) action performed by Rempel (2014). The snapshot model used corresponds to the stationary stage and has a vertical unsigned flux density $\langle |B_z| \rangle = 80$ G in the visible surface layers and zero net magnetic flux. The original dimensions of the snapshot are $6.144 \times 6.144 \times 3.072$ Mm³ with $8 \times 8 \times 8$ km resolution. This 3D model was interpolated to a coarser grid of $77 \times 77 \times 102$ points to facilitate the NLTE radiative transfer calculations. The resulting snapshot model has 80 km resolution in the horizontal directions and 8 km resolution in the vertical direction. Given that the Si I 10 827 Å line originates in the upper solar photosphere, we use only the uppermost ~ 0.8 Mm layer for our radiative transfer calculations.

Figure 1 shows the height variation of the temperature T_Z , of the vertical magnetic field strength B_Z and of the vertical velocity V_Z along one of the vertical slices of the snapshot.

Figure 2 illustrates the height dependence of the mean temperature in the lower photosphere ($\log_{10} \tau_5 < -0.5$). We note, that the mean temperature in the MHD snapshot models of Rempel (2014) and Vögler & Schüssler (2007) agree very well with the temperature of the 1D semi-empirical model MACKKL (Maltby et al. 1986) based on observations of the continuum radiation. As a result, the absolute continuum intensities at different wavelengths computed in the 3D snapshot model of Rempel (2014) are consistent with those calculated in the MACKKL model (see Shchukina & Trujillo Bueno 2015). At heights above $\log_{10} \tau_5 > -0.5$, the above-mentioned 3D MHD snapshot models are significantly cooler compared to the MACKKL model. It is interesting to note that the 3D model of Asplund et al. (2000), which results from purely hydrodynamical simulations, has a temperature lower than that of the MACKKL model up to the $\log_{10} \tau_5 \approx -2$ height. Above this height, the 3D model of Asplund et al. (2000) is hotter.

2.2. Method

We solved the NLTE formation problem of the Si I 10 827 Å line in the 3D MHD model atmosphere of Rempel (2014) mentioned above, neglecting the effects of horizontal radiative transfer (i.e., we applied the so-called 1.5D approximation).

We obtained the self-consistent solution of the statistical and radiative transfer equations applying an efficient multilevel transfer code developed by Shchukina & Trujillo Bueno (2001) to facilitate NLTE radiative transfer simulations with very complex atomic models. The code has been used before for the NLTE interpretation of iron, strontium, oxygen, barium, titanium, and silicon solar spectra (Shchukina & Trujillo Bueno 2001, 2009, 2011; Shchukina et al. 2005, 2009, 2012; Kostyk et al. 2006; Kostyk & Shchukina 2004; Khomenko et al. 2001; Trujillo Bueno et al. 2004; Trujillo Bueno & Shchukina 2007; Sukhorukov 2012; Sukhorukov & Shchukina 2012). The code is based on efficient iterative methods (see Trujillo Bueno & Fabiani Bendicho 1995; Socas-Navarro & Trujillo Bueno 1997, and more references therein) that allow a fast and accurate solution of NLTE radiative transfer problems.

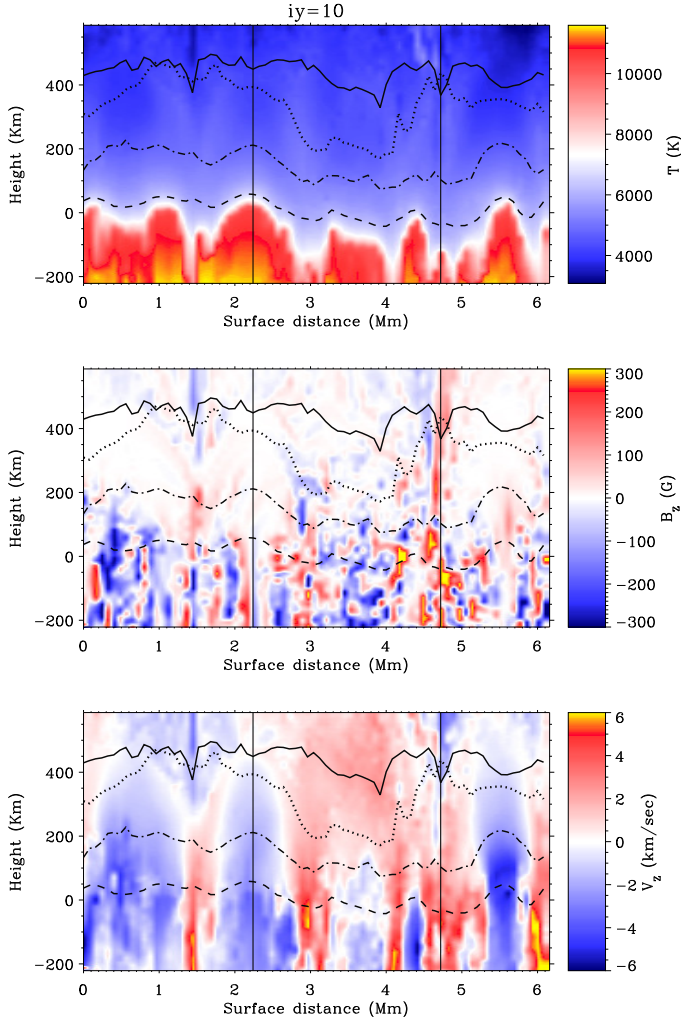


Fig. 1. Top panel: height variation of the temperature along the slice corresponding to the spatial grid point $iy = 10$ in the 3D snapshot model with vertical unsigned flux density $\langle |B_z| \rangle = 80$ G. Middle panel: height variation of the vertical magnetic field strength B_z along the same slice. Bottom panel: height variation of the vertical velocity v_z . Curves show the horizontal fluctuations of the formation height $H_{\Delta\lambda}$ of the Si I 10 827 Å line derived using the Eddington-Barbier approximation. Thick solid curve: $\Delta\lambda = 0$; dotted curve: $\Delta\lambda = -0.08$ Å; dash-dotted curve: $\Delta\lambda = -0.2$ Å. Dashed curve indicates the formation height of the line continuum. Two vertical lines correspond to the grid points $ix = 28$ (a granule) and $ix = 59$ (an intergranule).

We used the field-free population departure coefficients β of the lower and upper levels of the Si I 10 827 Å line, obtained from the self-consistent solution of the statistical and radiative transfer equations, as input for the the Stokes-vector formal solver. We define the departure coefficients as $\beta = n_{\text{NLTE}}/n_{\text{LTE}}$ with the NLTE and LTE atomic level populations denoted by n_{NLTE} and n_{LTE} , respectively.

We calculated the emergent Stokes profiles applying a radiative transfer code based on the DELOPAR method proposed by Trujillo Bueno (2003) and solving the Zeeman line transfer problem neglecting atomic level polarization (see Trujillo Bueno & Landi Degl'Innocenti 1996, and more references therein). We believe this is a suitable approximation for calculating the disk-center Stokes profiles of the Si I 10 827 Å line because high-sensitivity spectropolarimetric observations of

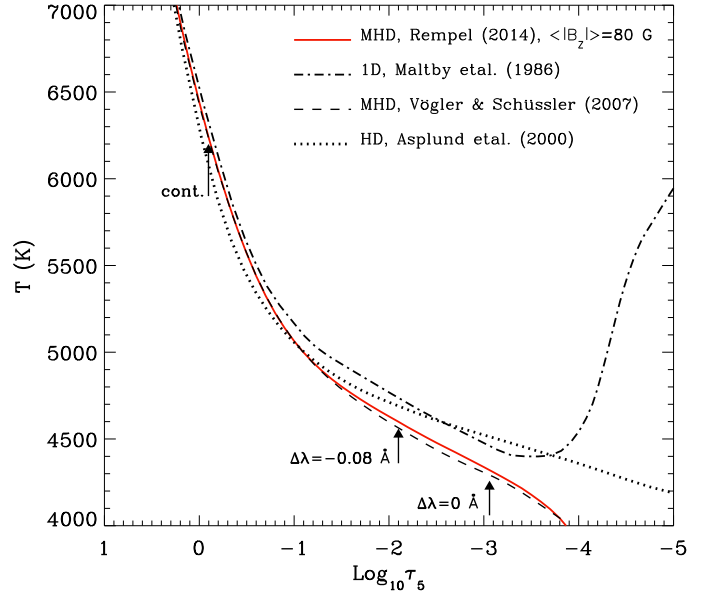


Fig. 2. Variation with optical depth $\log_{10} \tau_5$ of the temperature in the 3D model and in the MACKKL 1D semi-empirical model of the solar atmosphere. The temperature values in the 3D snapshots resulting from the magneto-convection simulations with small-scale dynamo action by Rempel (2014), Vögler & Schüssler (2007), and the hydrodynamic simulations by Asplund et al. (2000) correspond to the horizontal averages at each optical depth τ_5 . Arrows mark the mean optical depths of formation $\log_{10} \langle \tau_5 \rangle$ for three wavelength points $\Delta\lambda$ within the Si I 10 827 Å line, calculated using the $\langle |B_z| \rangle = 80$ G 3D snapshot model.

quiet regions close to the solar limb do not seem to show any hint of scattering polarization in this line (e.g., Centeno et al. 2010). Very likely, elastic collisions with neutral hydrogen atoms significantly depolarize the levels of the Si I 10 827 Å line in its region of formation.

We calculated the NLTE and LTE emergent Stokes I , Q , U , and V profiles for the Si I 10 827 Å line with a spectral resolution of $\Delta\lambda = 10$ mÅ for every (x, y) vertical column of the 3D MHD snapshot. We focus on the solar disc center case corresponding to a line of sight with $\mu = \cos \Theta = 1$ (with Θ the heliocentric angle). For the Si I 10 827 Å line, we assumed complete frequency redistribution. We normalized the Stokes profiles to the mean continuum intensity $\langle I_c \rangle$ obtained by averaging over the snapshot's horizontal direction. We used the mean continuum intensity to distinguish between granular and intergranular regions. An (x, y) -point belongs to a granule if its continuum intensity $I_c(x, y)$ is larger than the mean continuum intensity $\langle I_c \rangle$. The opposite is true for an intergranular lane.

We estimated the formation heights of the Si I 10 827 Å line in the $\langle |B_z| \rangle = 80$ G snapshot using the concept of “Eddington-Barbier height of line formation”. For a given wavelength $\Delta\lambda$ within the line, and at each (x, y) -point, we calculated the height $H_{\Delta\lambda}$ and the corresponding continuum optical depth $\tau_5(\Delta\lambda)$ at 5000 Å, where the line optical depth $\tau_{\Delta\lambda}$ is equal to unity. We did this for both the NLTE and LTE cases. Mean values of $\langle H \rangle$ and $\langle \tau_5 \rangle$ for each $\Delta\lambda$ -point were computed by averaging the corresponding quantities along the horizontal directions. The results of these calculations for the line continuum and the wavelength points $\Delta\lambda = 0$ (the line core) and $\Delta\lambda = -0.08$ Å are shown in Figs. 1 to 3. Figure 1 indicates that the formation heights $H_{\Delta\lambda}$ of the Si I 10 827 Å line fluctuate greatly across the surface

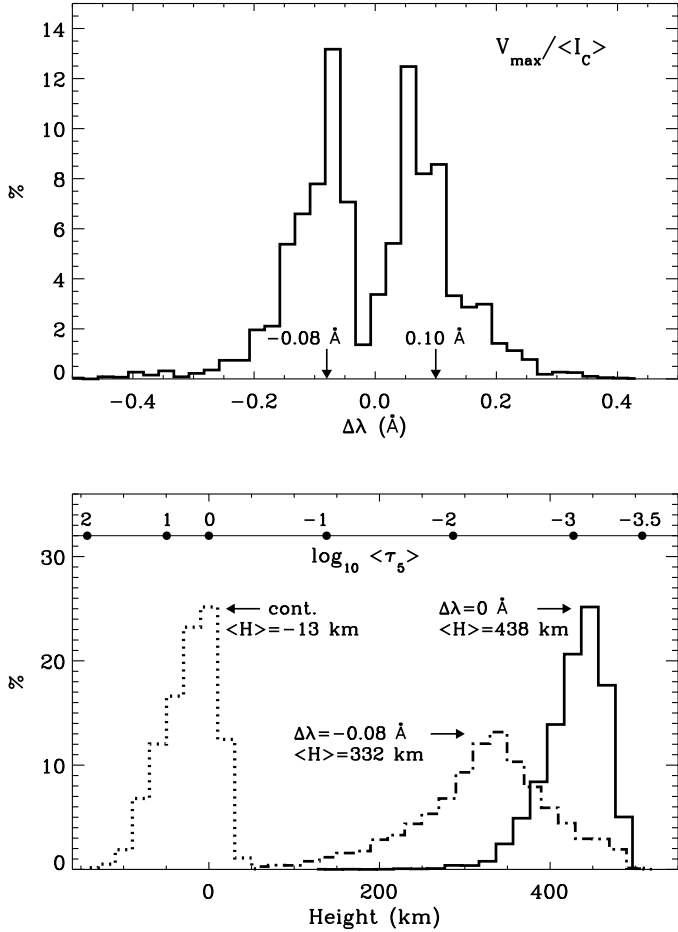


Fig. 3. Top panel: a histogram of the wavelength $\Delta\lambda$ positions of the NLTE Stokes V amplitude of the Si I 10 827 Å line. Arrows and numbers indicate the mean wavelength position of this amplitude in the left and right wings of the line. Bottom panel: histograms of the NLTE heights of formation $H_{\Delta\lambda}(\text{NLTE})$ calculated for three wavelengths within the Si I 10 827 Å line intensity profile. The mean heights of formation $\langle H \rangle$ are shown near each of the histograms. Values of $H_{\Delta\lambda}(\text{NLTE})$ represent the heights, where the NLTE optical depth at a given line wavelength $\Delta\lambda$ is equal to unity: $\tau_{\Delta\lambda}(\text{NLTE}) = 1$. The histograms have been calculated using the 3D snapshot with $\langle |B_z| \rangle = 80$ G and the simplest Si I model with six bb transitions (see the left bottom panel of Fig. 4). The top horizontal axis gives the mean optical depths $\log_{10}\langle\tau_5\rangle$ corresponding to the heights shown in the bottom horizontal axis. The scaling factor $S_H = 0.1$.

of the snapshot. The line formation region, as it follows from Fig. 2, covers a large portion of the photosphere, starting from the bottom of the photosphere (the line continuum) and ending near the temperature minimum (the line core). Histograms of the $H_{\Delta\lambda}$ values calculated for all (x, y) -grid points are shown in the bottom panel of Fig. 3.

For all (x, y) -grid points of the snapshot, we determined the wavelength positions $\Delta\lambda$ of the Stokes V profile peaks. We identify these peaks with the maximum absolute values of the Stokes profiles. A histogram of these $\Delta\lambda$ positions is shown in the top panel of Fig. 3. Note that the mean values of the Stokes V blue and red lobe peaks of the Si I 10 827 Å line are slightly different, being equal to -0.08 Å and 0.1 Å, respectively. We also calculated the wavelength positions of the Stokes Q and U profile peaks. On average, these peaks are located around ± 0.11 Å.

2.3. Atomic data

The most comprehensive model atom of silicon used in our study has 206 atomic energy levels of Si I, 89 levels of Si II, and one ground level of Si III, including their term and multiplet fine structure. The Si I and Si II levels are connected by 4708 bound-bound (bb) radiative transitions. In this model, each level is coupled to its parent level of the next ionization stage by bound-free (bf) radiative transitions. The number of the bf transitions is 295. The Si I term diagram is, in fact, complete up to excitation potential EP = 8 eV. The Si II term diagram includes all levels with excitation energies EP < 7.7 eV measured relative to the Si II ground state. We show this model in the top panels of Fig. 4.

This comprehensive atomic model serves as a standard against which our less detailed working models are tested. The most complicated atomic model is shown in the bottom left panel of Fig. 4. It contains the same number of Si I levels (206) as the comprehensive model, three parent levels $3p^2P_0^{+}$, $3p^2P_3^{-}$, and $3p^4P_{1/2}$ of Si II, and the ground level $3s^1S_1$ of Si III. We excluded all Si II lines and weak Si I lines with oscillator strengths $f < 10^{-4}$. Finally, we reduced the number of bb radiative transitions to 605. The simplest working model (bottom right panel of Fig. 4) has six bb radiative transitions between fine structure levels of the $4s^3P^0$ (lower) and $4p^3P$ (upper) terms of Si I. One of these transitions, namely $4s^3P_2^0 - 4p^3P_2$, gives rise to the Si I 10 827 Å line. In addition to the levels mentioned above, the simplest model includes the levels that play an important role for the ionization balance. They are low-excitation meta-stable levels of Si I lying below the $4s^3P^0$ term, including their corresponding parent levels in the next ionization stage of Si II. In total, the simplest model has twelve atomic energy levels of Si I, three levels from the $3p^2P^0$ and $3p^4P$ terms of Si II, the ground level $3s^1S_1$ of Si III, and fifteen bf radiative transitions. We point out that this model, in fact, corresponds to the case of the equivalent two-level atom with continuum (see Mihalas 1978). The levels of the simplest silicon model atom including their excitation E_{exc} and ionization energies E_{ion} as well as photo-ionization cross-sections at threshold σ_T are specified in Table 1. The six lines of this model are listed in Table 2.

The atomic model and data, including the oscillator strengths, bf cross-sections, collisional rates, etc., are described in detail by Sukhorukov & Shchukina (2012), Shchukina et al. (2012) and Sukhorukov (2012). In this paper, we briefly summarize the following.

Oscillator strengths, $\log gf$ (i.e., the logarithm of the absorption oscillator strength f multiplied by the statistical weight g of the lower level), for bound-bound radiative transitions were taken from several sources: Experimental measurements of Garz (1973) and Becker et al. (1980), solar oscillator strengths of Gurtenko & Kostik (1989) and Borrero et al. (2003), theoretical estimates by Kurucz (1995) and compilations from the VALD database (Kupka et al. 1999). The Si I 10 827 Å line is synthesized with $\log gf = 0.239$ taken from Froese-Fischer (2005). In the 3D HD model by Asplund et al. (2000), this value gives the best agreement between theoretical and observed profiles of this line (Sukhorukov 2012).

The rates of collisional inelastic excitation by electrons for allowed transitions were derived using the formula of van Regemorter (1962). For forbidden transitions, we applied the impact parameter approximation of Seaton described in Bely & Regemorter (1970). The collisional strength Ω used in this approximation was taken equal to unity for all these transitions (see Allen 1973, and more details therein). This approximation provides a suitable representation of the full matrix of

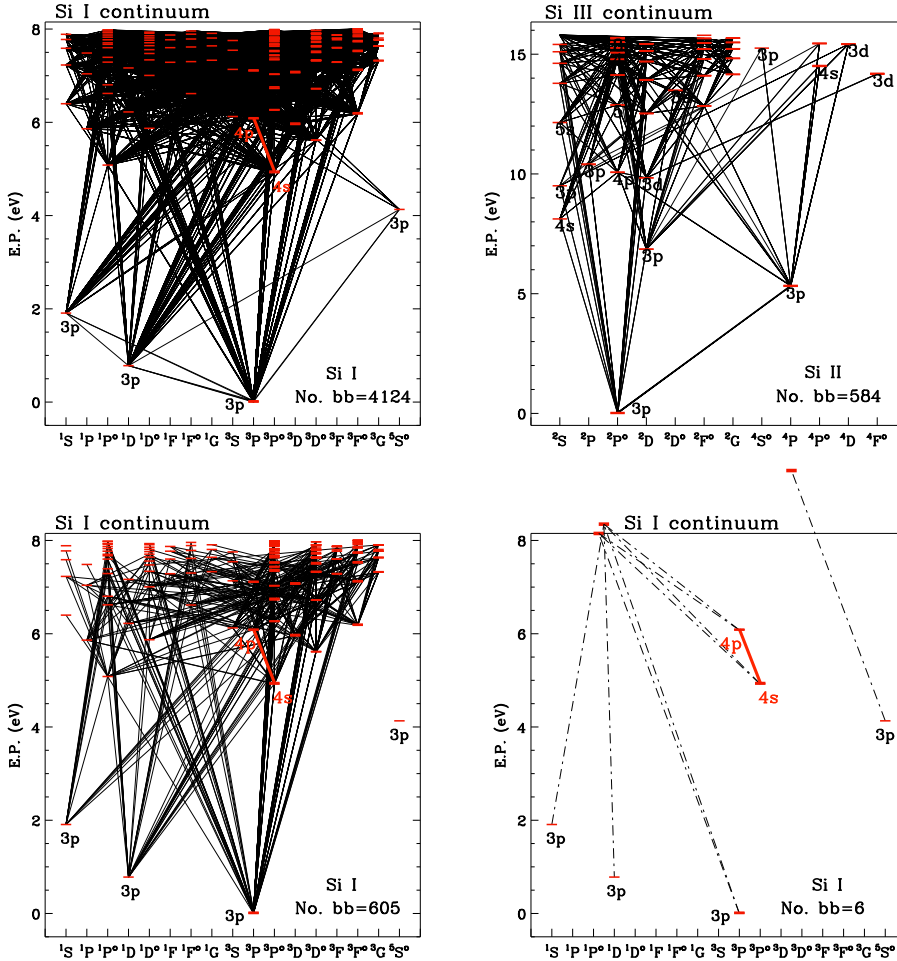


Fig. 4. Diagram of the energy levels (red horizontal bars) and radiative transitions for the different model atoms of silicon. The number of bound-bound transitions in each model is indicated in the lower right corner of the panels. *Top panel:* the full, comprehensive model of Si I + Si II atom. Note that the diagrams for the Si I and Si II atoms are shown separately. *Bottom panels:* the Si I working model with 605 bb transitions (*left*) and the simplest one (*right*) with six bb transitions between the fine structure levels of the Si I lower $4s^3P^0$ and upper $4p^3P$ terms. These bb transitions are marked by a thick red line. One of these transitions ($4s^3P^0_2 - 4p^3P_2$) gives rise to the Si I 10 827 Å line. Solid and dashed-dotted lines indicate, respectively, bb and bf radiative transitions. The bf transitions are shown only for the simplest model. See the main text for further information.

electron excitation rates since it correctly describes their evolution with the excitation energy of the bound-bound transitions.

The photoionization cross-sections for most of the bound-free transitions were taken from the TOPBase server (Cunto et al. 1993). For the Si I atom they were calculated by Nahar & Pradhan (1993) applying the close coupling approach and the R-matrix method. The photoionization cross-sections for Si II were computed by Mendoza et al. (1995) using the close-coupling approach in LS-coupling. These cross-sections are sampled on a very-fine-frequency grid with thousands of points in order to resolve resonance peaks resulting from autoionization transitions. We smoothed and interpolated the original photoionization data following the strategy of Bautista (1998). For the bound-free photoionization transitions whose cross-sections are not available in the TOPBase, we used the hydrogen-like approximation.

In our calculations, we included inelastic collisions with hydrogen atoms. Due to the lack of reliable quantum-mechanical calculations, we used the semi-empirical formula of Drawin (1968, 1969) with a scaling factor S_H . At present, the magnitude of this factor is still under debate (see Shchukina & Trujillo Bueno 2001 Bard & Carlsson 2008; Shi et al. 2008; Sukhorukov 2012, and more references therein). We note, that the semi-empirical scaling factor S_H is model atmosphere dependent. In the 3D HD model by Asplund et al. (2000), a good agreement of the theoretical NLTE Si I 10 827 Å line profile with observations can be obtained with $S_H = 0.1$ (Sukhorukov 2012) while in the 1D case, a better agreement can be obtained using $S_H = 1$ (Shi et al. 2008; Sukhorukov 2012).

We used the Voigt function for the line absorption profile with the damping constant γ defined as the sum of the Van der Waals broadening γ_V and the radiative broadening γ_{rad} . The main contribution to γ gives Van der Waals broadening by H I and He I atoms and H₂ molecules. For the Si I 10 827 Å line, we evaluated the damping constant γ_V using the semi-classical theory of Anstee, Barklem, and O'Mara (see Anstee & O'Mara 1995; Barklem & O'Mara 1997; Barklem et al. 1998, and references therein) known as the ABO theory. For the other lines, we applied the classical Eq. (82, 48) of Unsöld (1955) with an enhancement factor $E = 2.5$. According to Shchukina et al. (2012), the ABO theory and the Unsöld's equation with such a value of E give, on average, very similar results.

We used a solar silicon abundance $A_{Si} = 7.55$ recommended by Grevesse & Sauval (1998). This value agrees with the recent silicon abundance obtained by Shchukina et al. (2012) through a NLTE spectral synthesis in the 3D HD model of the solar surface convection (Asplund et al. 2000).

We are aware that the results of our NLTE modeling of the Si I 10 827 Å line are sensitive to uncertainties in different atomic parameters such as the oscillator strengths, collisional strengths, bf cross-sections, and the enhancement factor and so on. The errors in the NLTE solution for the Si I 10 827 Å line caused by these uncertainties were estimated in several studies (e.g., Bard & Carlsson 2008; Shi et al. 2008; Sukhorukov & Shchukina 2012; Shchukina et al. 2012; Sukhorukov 2012, and references therein). As we know from them, the largest errors occur, first of all, due to uncertainties in the electron and hydrogen collisional rates. Moreover,

Table 1. Levels of the sixteen-level silicon model atom.

Nr	Atom	Level	g	E_{exc} [cm $^{-1}$]	E_{ion} [eV]	σ_T [Mb]
1	Si I	3p 3P_0	1.0	0.000	8.152	7.70
2	Si I	3p 3P_1	3.0	77.115	8.142	23.12
3	Si I	3p 3P_2	5.0	223.157	8.160	38.46
4	Si I	3p 1D_2	5.0	6298.850	7.406	35.25
5	Si I	3p 1S_0	1.0	15 394.370	6.279	22.22
6	Si I	3p $^5S_2^o$	5.0	33 326.053	9.329	52.43
7	Si I	4s $^3P_0^o$	1.0	39 683.163	3.232	0.05
8	Si I	4s $^3P_1^o$	3.0	39 760.285	3.222	0.14
9	Si I	4s $^3P_2^o$	5.0	39 955.053	3.234	0.23
10	Si I	4p 3P_0	1.0	49 028.294	2.073	1.75
11	Si I	4p 3P_1	3.0	49 060.601	2.069	5.26
12	Si I	4p 3P_2	5.0	49 188.617	2.089	8.74
13	Si II	3p $^2P_{1/2}^o$	2.0	65 747.760	16.346	0.58
14	Si II	3p $^2P_{3/2}^o$	4.0	66 035.000	16.310	1.16
15	Si II	3p $^4P_{1/2}$	2.0	108 572.050	11.036	1.42
16	Si III	3s 1S_0	1.0	197 585.900	33.493	

Table 2. Lines of the sixteen-level silicon model atom.

up–low	Transition	Wavelength Å	f_{lu}
11–7	4p 3P_1 –4s $^3P_0^o$	10 660.973	4.467×10^{-1}
10–8	4p 3P_0 –4s $^3P_1^o$	10 786.849	1.342×10^{-1}
11–8	4p 3P_1 –4s $^3P_1^o$	10 749.378	2.046×10^{-1}
12–8	4p 3P_2 –4s $^3P_1^o$	10 603.425	1.169×10^{-1}
11–9	4p 3P_1 –4s $^3P_2^o$	10 979.309	5.141×10^{-2}
12–9	4p 3P_2 –4s $^3P_2^o$	10 827.089	3.470×10^{-1}

Sukhorukov (2012) have found that collisional effects are more important in the 3D HD model of the solar photosphere than in 1D semi-empirical models.

In the present work, we investigate the sensitivity of the NLTE solution to the uncertainties of the scaling factor S_H . Figure 5 shows spatially averaged NLTE profiles of the Si I 10 827 Å line calculated in the 3D MHD snapshot model with scaling factors $S_H = 0.1$ and $S_H = 1$. We reach the best agreement with observations with $S_H = 1$. This value is one order of magnitude larger than that used by Sukhorukov (2012) in the 3D model resulting from the hydrodynamic simulations of Asplund et al. (2000). Since the NLTE profiles in the MHD and HD snapshots were calculated using virtually the same atomic parameters, this disagreement can only originate from differences in the temperature structure of the snapshots under consideration. Figure 2 shows that in formation layers of the Si I 10 827 Å line, the 3D MHD model of Rempel (2014) is significantly cooler compared to the purely hydrodynamic model of Asplund et al. (2000). Thus, in the NLTE modeling of this line, the S_H factor has nothing to do with the semi-empirical approach developed by Drawin (1968, 1969), and serves only as a masking parameter that hides temperature uncertainties in the model atmosphere used. Further in this paper we present the results only for $S_H = 0.1$. We do so in order to demonstrate the maximum NLTE effects in the Si I 10 827 Å line that can be expected in the Rempel’s model.

We have not studied how the uncertainties of the electron collisional strengths affect the NLTE solution assuming that the

major contributors to the matrix of electron collisional rates are forbidden transitions for which the value of Ω is close to unity. For this type of transition, approximations of $\Omega = 0.1$ or $\Omega = 10$, respectively, underestimate or overestimate the collisional rates by roughly an order of magnitude (Allen 1973). For this reason, we always use $\Omega = 1$ for forbidden transition in our NLTE calculations.

3. Results

3.1. The departure coefficients and the line source function for the Stokes parameter I

Figure 6 shows the population departure coefficients β and the line source function S_{lu} for the Stokes I parameter of the Si I 10 827 Å line calculated in typical 1D granular and intergranular models associated to two spatial grid points, ($ix = 28$, $iy = 10$) and ($ix = 59$, $iy = 10$), respectively. The behavior of the β -coefficients and the line source function shown in Fig. 6 is a result of the interaction of several NLTE mechanisms described in detail by Bruls et al. (1992), Carlsson et al. (1992), Shchukina & Trujillo Bueno (2001), Bard & Carlsson (2008). Here we simply point out the most important ones: Line scattering and photon losses, ultraviolet (UV) line pumping, ultraviolet overionization, and over-recombination associated with the photon suction mechanism.

The line scattering and photon losses manifest themselves as a divergence of the β -coefficients of the lower 4s $^3P_2^o$ and the

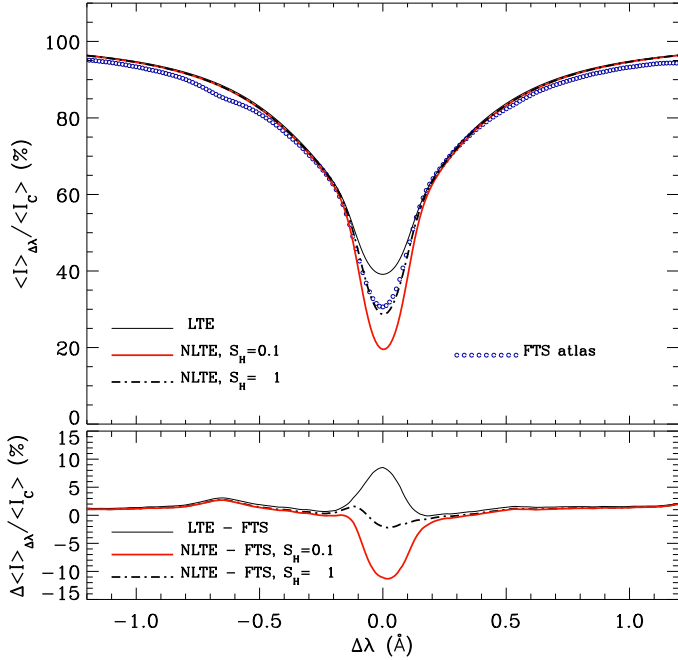


Fig. 5. Top panel: calculated and observed intensity profiles of the Si I 10827 Å line corresponding to the disk-center. Solid red and dashed-dotted black lines: spatially averaged NLTE profiles calculated in the 3D MHD snapshot, respectively, with a scaling factor $S_H = 0.1$ and $S_H = 1$. Thin solid line: the LTE profile. Small open blue circles: the observed profile from the FTS atlas (Neckel & Labs 1984; Neckel 1999). Bottom panel: differences between the synthetic and the observed profiles. The NLTE profiles are calculated using the simplest Si I model with six bb transitions (see Fig. 4, bottom right panel).

upper $4p\ ^3P_2$ levels of the the Si I 10827 Å line. Such a divergence results from the photon losses near the layer where the optical depth is unity. Scattering propagates the photon losses far below this layer. In the photosphere, the photon suction mechanism produces an excess of Si I atoms in the lower level of the Si I 10827 Å line, while the pumping by numerous low-excitation UV lines of Si I leads to their overpopulation in the upper photosphere. The UV overionization depopulates both the lower and the upper levels. This overionization is caused by the “hot” UV continuum radiation that exceeds the Planck function starting from the lower photospheric layers.

To quantify the NLTE mechanisms in the Si I 10827 Å line, we compare two approximations for the source function S_{lu} of the Stokes- I parameter of this line. Generally, the line source function for the multilevel atom can be quite accurately described using the equivalent two-level approach. In this case (see Mihalas 1978)

$$S_{lu} = \frac{\bar{J}_{lu} + \varepsilon' + \theta \cdot B}{1 + \varepsilon' + \eta}, \quad (1)$$

with $\bar{J}_{lu} = \int \phi_\nu J_\nu d\nu$ the mean intensity averaged over line profile, ϕ_ν the normalized absorption profile, B the Planck function, ε' the ratio of collisional to radiative de-excitation for the lower l and the upper u levels of the line, and η and $\theta \cdot B$ the interlocking terms, which represent the degree of the collisional and radiative coupling of the levels under consideration with all the other levels of the atom.

The other approximation for the source function, known as the two-level atom approach, considers the simplest atomic

model consisting of two levels, l and u between which only radiative transitions can occur. In this case,

$$S_{lu} = \bar{J}_{lu}. \quad (2)$$

By comparing the line source functions for the Si I atomic models shown in Fig. 4 with approximation (2) we can estimate the cumulative NLTE effects produced by the ε' , η , and $\theta \cdot B$ terms in Eq. (1). We show the results of this comparison in the bottom panels of Fig. 6. We clearly see that even for the simplest atomic model, the line source function S_{lu} of the Si I 10827 Å line significantly exceeds the mean intensity \bar{J}_{lu} . In other words, the radiative and collisional coupling of the Si I 10827 Å line levels with continuum is very important and must necessarily be taken into account. Figure 6 also demonstrates that in the case of more complicated Si I model atoms, such as those in the left panels of Fig. 4, the collisional and radiative coupling of the lower and upper levels of this line with all the other Si I levels causes a further, although relatively slight, increase in the line source function, and it deviates significantly from the Planck function B above 300 km.

It is interesting to note, that taking these interlocking effects into account results in a significant overpopulation of the lower $4s\ ^3P_0$ and the upper $4p\ ^3P_2$ levels of the Si I 10827 Å line above 500 km. The peak in the population departure coefficients shown in the upper panels of Fig. 6 is due to an excess in the UV continuum radiation field near 2500 Å, which leads to a radiative pumping of the lower level via the wings of UV resonance lines of Si I.

To quantify further the deviation of the line source function S_{lu} of the Si I 10827 Å line from the Planck function, we calculated the excitation temperature T_{ex} at the LTE height of formation of the line center. The excitation temperature is derived from the following equation:

$$\begin{aligned} S_{lu} &= \frac{2h\nu_0^3}{c^2} \frac{1}{(\beta_l/\beta_u) \exp(h\nu_0/kT_e) - 1} \\ &= \frac{2h\nu_0^3}{c^2} \frac{1}{\exp(h\nu_0/kT_{ex}) - 1}, \end{aligned} \quad (3)$$

with T_e the electron temperature at the same height ν_0 the line center frequency.

The top panel of Fig. 7 shows the difference between the excitation temperature T_{ex} and the electron temperature T_e along the surface line $jy = 10$ calculated using the three different silicon atomic models. We note that results obtained for the other jy surface lines are similar to those shown in Fig. 7. As seen in this panel, in the formation layers of the Si I 10827 Å line (no matter how complex the model atom is), the excitation temperature is always lower than the electron temperature. The difference $T_{ex} - T_e$ varies from -200 K to -800 K along the snapshot surface.

The bottom panel of Fig. 7 quantifies the errors in the excitation temperature caused by using the simplest working model of the Si I atom instead of the comprehensive one. As seen, these errors are relatively small, mainly ranging between -50 K and -100 K. Interestingly, the excitation temperatures obtained using the comprehensive model and the working model with 605 bb transitions (see the left bottom panel of Fig. 4) are close to one another. On average, the difference between them does not exceed 30 K.

Finally, we conclude that the LTE diagnostics based on an analysis of the Si I 10827 Å line could significantly underestimate the electron temperature in the formation layers of this line.

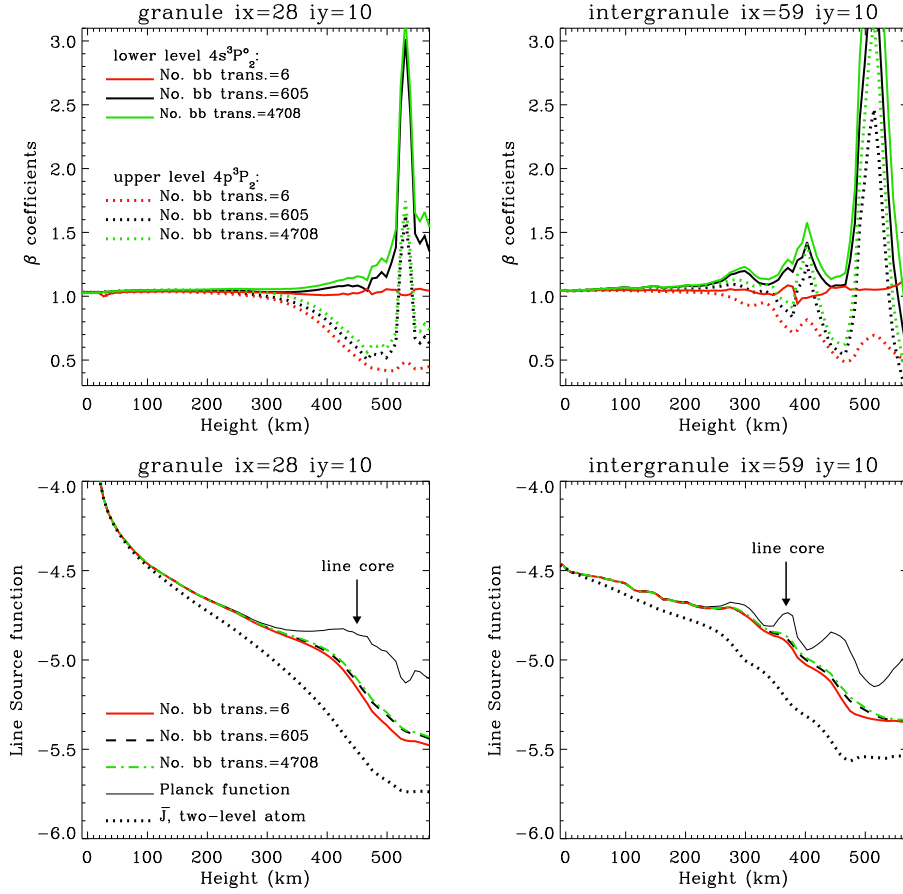


Fig. 6. Top panels: departure coefficients β for the lower $4s^3P_2^o$ (solid lines) and the upper $4p^3P_2$ (dashed lines) levels of the Si I 10 827 Å line plotted against the atmospheric height. Bottom panels: the line source function S_{lu} for the Stokes parameter I of the Si I 10 827 Å line versus height. The left and right panels show results for the granular and intergranular 1D models corresponding, respectively, to the spatial grid points ($ix = 28, iy = 10$) and ($ix = 59, iy = 10$) in the $\langle |B_z| \rangle = 80$ G snapshot. Arrows mark the formation heights of the line core. The curves of different colors indicate the β and S_{lu} values calculated using three different atomic models of the silicon atom. The black dotted curve shows the line source function for the two-level atom approximation, which is equal to the mean intensity \bar{J}_{lu} averaged over the line profile. The black thin solid curve shows the Planck function. The scaling factor $S_H = 0.1$.

3.2. Formation heights

The top panels of Fig. 6 demonstrate that in the photospheric layers, the departure coefficient β_l of the lower level of the Si I 10 827 Å line is above unity. Since this level is overpopulated ($\beta_l > 1$), the line opacity grows and, as a result, the Si I 10 827 Å line is formed higher than in LTE. We note that the lower level of the Si I 10 827 Å line tends to be more overpopulated with an increasing complexity of the silicon atomic model. So, for a more complicated atomic model, the height shift caused by NLTE effects on the line opacity has to be larger.

The top panel of Fig. 8 shows a variation in the shift of the height of formation $\Delta H_0(\text{NLTE}) = H_0(\text{NLTE}) - H_0(\text{LTE})$ of the Si I 10 827 Å line center along the $iy = 10$ surface line of the snapshot caused by the NLTE effects on the line opacity. We note that results for other surface lines are very similar. The bottom panel of this figure displays the errors ΔH in the height of formation that are caused by using the working models of the silicon atom instead of the comprehensive one.

The results presented in the top panel clearly indicate that the $\Delta H_0(\text{NLTE})$ values increase as the silicon atomic model becomes more and more complicated. However, the NLTE shifts in the height of formation of the Si I 10 827 Å line center never exceed 40 km. Generally, we found that for the Si I 10 827 Å line, the NLTE shifts of the formation height are always positive and are less than a few tens of kilometers along the whole surface of the snapshot.

As we see in the bottom panel, the errors ΔH in the height of formation caused by using the working model of the Si I atom with 605 bb transitions instead of the comprehensive model of

Si I + Si II atom are only a few kilometers. Using the simplest working atom leads to slightly larger errors.

We note, that the NLTE effects in the Si I 10 827 Å line opacity produce slightly deeper line profiles as compared with the case of a zero shift in the height of formation because, due to a positive shift of the formation height, this line is formed higher in the solar photosphere where the line source function is lower.

Summarizing, we would like to draw attention to the following points. Small errors in the NLTE height of formation and the line source function of the Si I 10 827 Å line caused by using the working model of the silicon atom with 605 bb radiative transitions instead of the comprehensive one is a good reason to use the former model as a reference in our further analysis.

3.3. The Stokes profiles

The left panels of Figs. 9 and 10 show LTE and NLTE emergent Stokes profiles $I_{\Delta\lambda}$, $Q_{\Delta\lambda}$, $U_{\Delta\lambda}$, and $V_{\Delta\lambda}$ across the Si I 10 827 Å line normalized to the spatially averaged continuum intensity $\langle I_c \rangle$. The NLTE Stokes parameters were calculated using the simplest Si I model atom with six bb radiative transitions (red solid line), the atomic model with 605 bb radiative transitions (black dashed line), and the comprehensive model (green dashed-dotted line). The results shown in these figures are interesting examples of granular and intergranular Stokes profiles obtained in the 3D MHD snapshot model. As seen in the figures, all Stokes profiles are strongly asymmetric. In addition, the linearly and circularly polarized line profiles have irregular shapes due to the changes of the magnetic field polarity along the line-of-sight in the presence of velocity gradients, as clearly seen in Fig. 1 (see also Khomenko et al. 2005, and references therein).

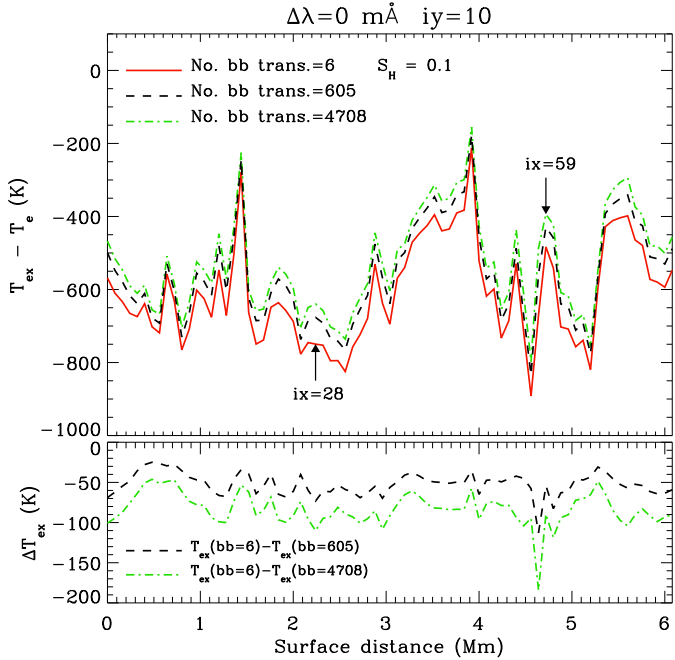


Fig. 7. Top panel: differences between the excitation temperature T_{ex} and the electron temperature T_e calculated for the Si I 10 827 Å line along the surface line $iy = 10$ in the 3D snapshot model with $\langle |B_z| \rangle = 80$ G. The T_{ex} and the T_e values are determined at the heights $H_0(\text{LTE})$ where the LTE optical depth at the line center $\tau_0(\text{LTE}) = 1$. Curves of different colors indicate results obtained using three silicon atomic models. Arrows show the grid points $ix = 28$ (the granule) and $ix = 59$ (the intergranule). Bottom panel: the differences ΔT_{ex} in the excitation temperature along the same surface line $iy = 10$ obtained by using different atomic models of the silicon atom. Dashed curve: the ΔT_{ex} values found by comparing the excitation temperatures computed from the simplest Si I model with six bb transitions and the Si I working model with 605 bb transitions. Dashed-dotted green curve: the ΔT_{ex} values obtained by comparing the simplest Si I model and the comprehensive Si I + Si II model with 4708 bb transitions.

Both in the granule and in the intergranular lane, the Stokes Q and U signals, which respond to the transversal component of the magnetic field and are approximately proportional to the square of the ratio between the Zeeman splitting and the line's width, are small and only slightly exceed a noise level typical for observations of 10^{-3} . The Stokes Q and U signals are larger in the granule because here the transversal component of the field is larger. The Stokes V signals, which respond to the longitudinal component of the magnetic field and are approximately proportional to the ratio between the Zeeman splitting and the line's width, have the largest amplitudes in the intergranular lanes, where the vertical field component is significantly larger than in the granule cell center.

Both in the granule and in the intergranular lane selected, the most significant NLTE versus LTE discrepancies occur for the Stokes intensity profile. The NLTE effects are most pronounced around the line core. Note that the LTE intensity profiles are more shallow. Differences between the NLTE and LTE Stokes Q , U , and V profiles are less evident because the Stokes Q , U , and V signals themselves are much smaller than the Stokes I signal. The NLTE effects on the polarization profiles are larger in the wings. A comparison of the NLTE Stokes profiles of the Si I 10 827 Å line calculated using different model atoms reveals that they are almost indistinguishable.

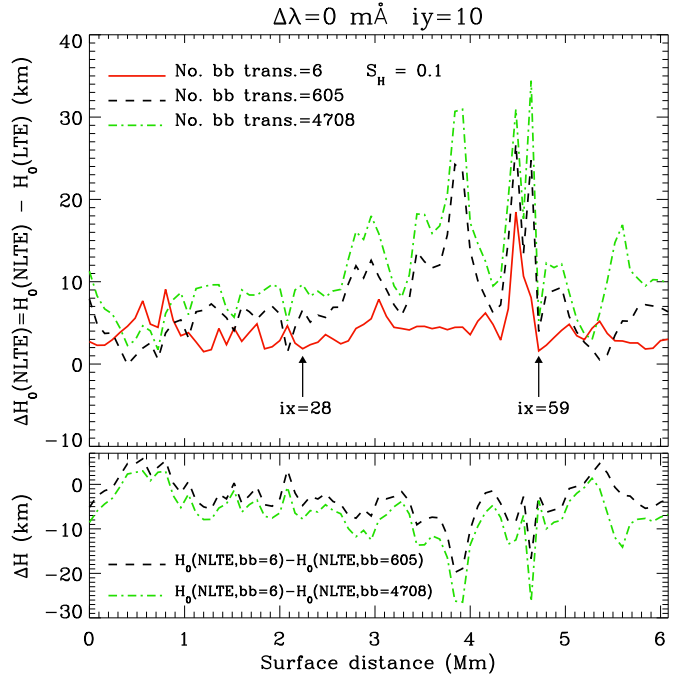


Fig. 8. Top panel: the shift of the height of formation $\Delta H_0(\text{NLTE}) = H_0(\text{NLTE}) - H_0(\text{LTE})$ of the Si I 10 827 Å line center ($\Delta\lambda = 0$) along the surface line $iy = 10$ in the 3D snapshot with $\langle |B_z| \rangle = 80$ G caused by the line opacity change due to the NLTE effects. Curves of different colours indicate results obtained using three different models of the silicon atom. Arrows mark the grid points $ix = 28$ (the granule) and $ix = 59$ (the intergranule). Bottom panel: the differences ΔH between the NLTE heights $H_0(\text{NLTE})$ of formation of the line center along the same surface line $iy = 10$ produced by using three different silicon model atoms. Dashed curve: the ΔH values found by comparing the $H_0(\text{NLTE})$ values for the simplest Si I model with six bb transitions and for the Si I working model with 605 bb transitions. Dash-dotted green curve: the ΔH values obtained by using the simplest Si I model and the comprehensive one with 4708 bb transitions.

The right panels of Figs. 9 and 10 quantify in detail the sensitivity of the Stokes profiles to the NLTE effects and to the choice of the model atom. The thin solid curves show the difference between the NLTE and LTE Stokes profiles calculated with the simplest model atom. The dashed-dotted curves show the differences between the NLTE profiles obtained using this atomic model instead of the comprehensive one, while the dashed curves quantify the comparison of the results obtained using the simplest model and the working model with 605 bb radiative transitions.

The top panels of these figures demonstrate that for the granule and intergranule selected, the errors in the Stokes I profiles of the Si I 10 827 Å line, caused by neglecting the NLTE effects, are significantly larger than the errors caused by using different atomic models. It is also noteworthy that for the same granule and intergranule, the impact of the effects associated with the choice of the atomic model on the Stokes Q , U , and V profiles may be comparable with the NLTE effects. The errors caused by these effects are small.

In order to further clarify the magnitude of the NLTE effects for the Si I 10 827 Å line we calculated the differences between the emergent NLTE and LTE Stokes profiles at a fixed wavelength $\Delta\lambda = 0.1$ Å for all surface (x, y) -grid points of the 3D snapshot model.

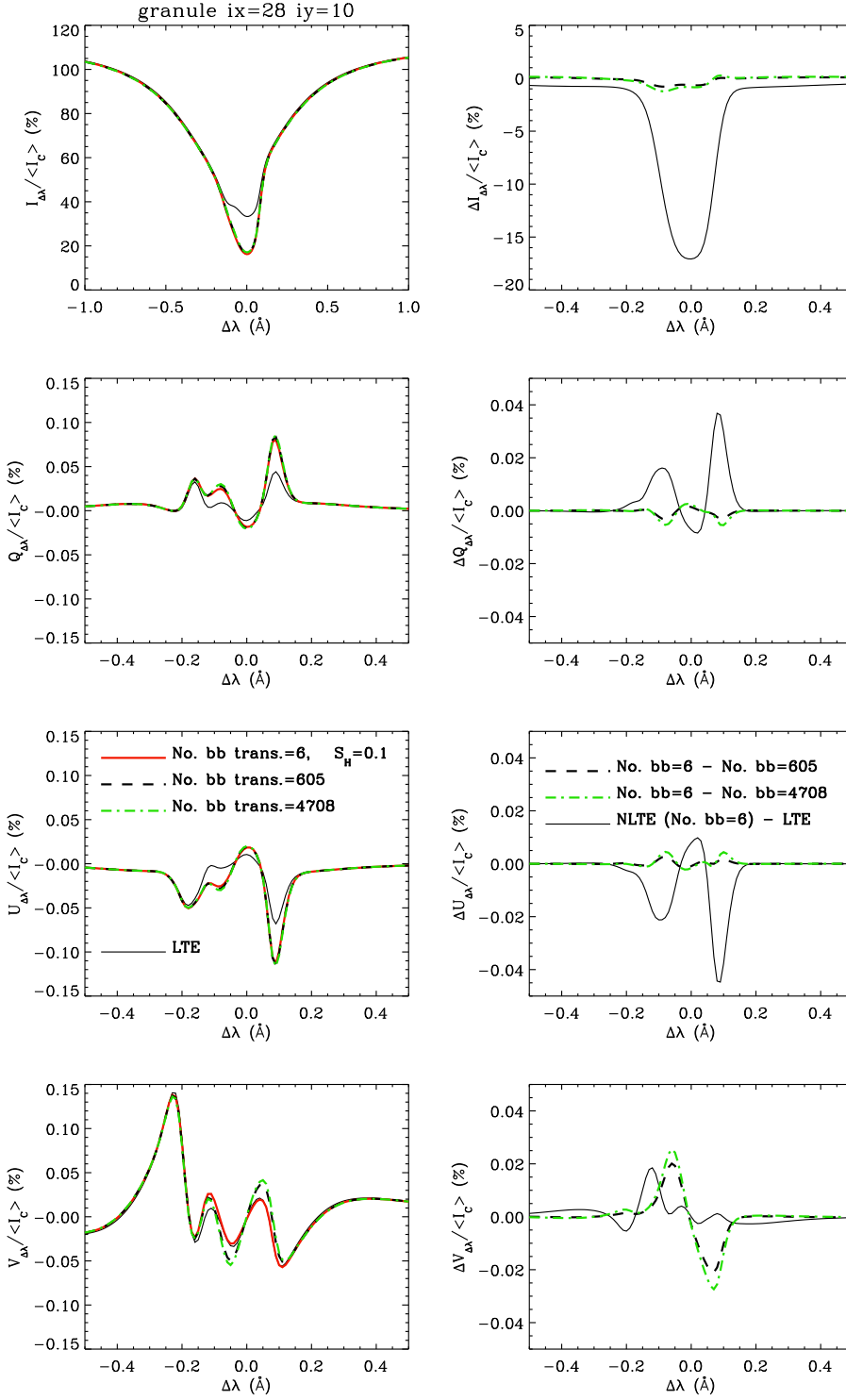


Fig. 9. Left, from top to bottom: the disk-center emergent Stokes profiles of the Si I 10 827 Å line for the granule model at the grid point $ix = 28$ and $iy = 10$ of the 3D snapshot model. Curves with different colors indicate the results for the three silicon model atoms (see Fig. 4). Thin solid line: LTE case. Right, from top to bottom: changes of the emergent Stokes parameters along the line profile caused by NLTE effects (thin solid curve) and by using the working atomic models instead of the simplest one. The NLTE effects are calculated by using the simplest working atomic model with six bb transitions. The dashed curve shows the results of comparing the NLTE profiles calculated by using the atomic models with six and 605 bb radiative transitions, while the green dash-dotted curve shows the same for the atomic models with six and 4708 bb radiative transitions. $S_H = 0.1$.

As follows from Fig. 3, the selected wavelength is close to the mean wavelength position of the peaks in the Stokes Q , U , and V profiles of this line. We note that at such a wavelength, the NLTE effects in the Stokes I profiles are still relatively large (see Figs. 5, 9, and 10).

Figure 11 shows results for all the Stokes I , Q , U , and V parameters (from top to bottom) obtained with the scaling factor $S_H = 0.1$. The left panels of the figure present surface maps of the Stokes profile changes at the wavelength $\Delta\lambda = 0.1 \text{ \AA}$ due to deviations from LTE, while the right panels display the scatter

of these changes plotted against the NLTE values of I , Q , U , and V at such a wavelength point. From this figure, we conclude the following.

The impact of NLTE effects on the intensity profiles of the Si I 10 827 Å line is very large, resulting in deeper profiles, in general. In the inner wings of the Stokes I profiles (i.e., close to the $\Delta\lambda = 0.1 \text{ \AA}$) the NLTE differences $[I(\text{NLTE}) - I(\text{LTE})]/\langle I_c \rangle$ vary in a wide range, from -34% to -1%. For the scaling factor $S_H = 1$, these differences become smaller but still remain large enough, that is, within the limits -20.4% and 3.2%. Despite the

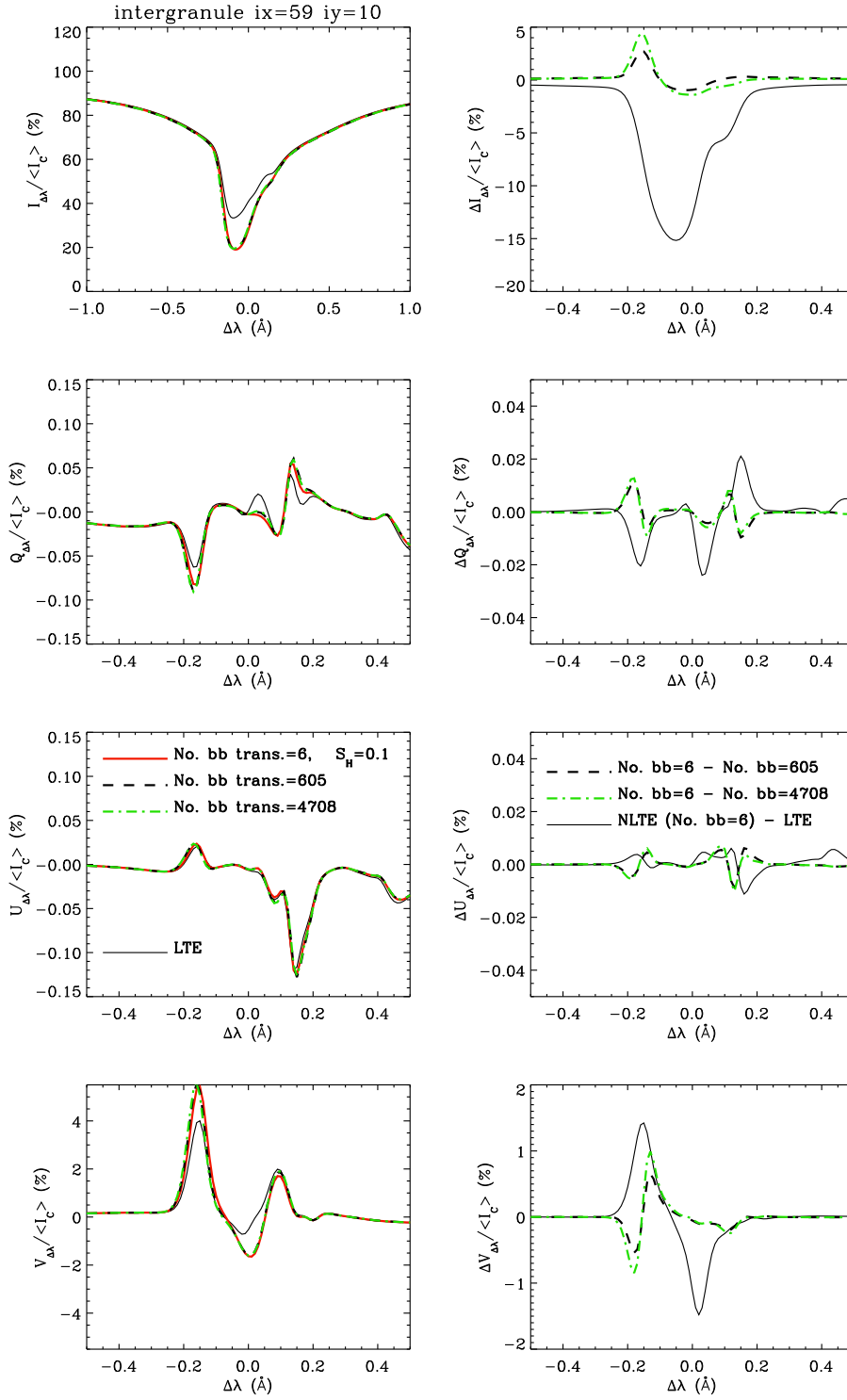


Fig. 10. Same as in Fig. 9, but for the intergranule model at the grid point $ix = 59$ and $iy = 10$.

large scatter, these differences have a well-pronounced dependence on the line residual intensity $I_{\Delta\lambda}/\langle I_c \rangle$ at the given wavelength (thick solid curve).

Variations of the NLTE effects for the Stokes Q , U , and V profiles along the surface of the 3D snapshot model are also very large. At the wavelength $\Delta\lambda = 0.1 \text{ \AA}$, where most of the Stokes Q , U , and V peaks occur, the differences between the NLTE and LTE Stokes profiles are comparable to the values of the Stokes signals themselves. The right panels of Fig. 11 demonstrate a clear trend: these differences increase with increasing Stokes Q , U , and V signals. At the same time, their scatter also

increases towards larger absolute Stokes amplitudes. An order of magnitude increase in the scaling factor S_H reduces the range of the NLTE changes for the Stokes Q , U , and V profiles by a factor two. Nevertheless, these changes are still relatively large and comparable to the values of Stokes signals themselves. For example, for the case $S_H = 1$, the changes of the Stokes V profile at $\Delta\lambda = 0.1 \text{ \AA}$ caused by NLTE effects lie between -5.6% and 6% .

Figure 12 shows that for the disk-center Stokes V profile, the magnitude of the NLTE effects correlates with the vertical component B_Z of the magnetic field vector in the formation layers of

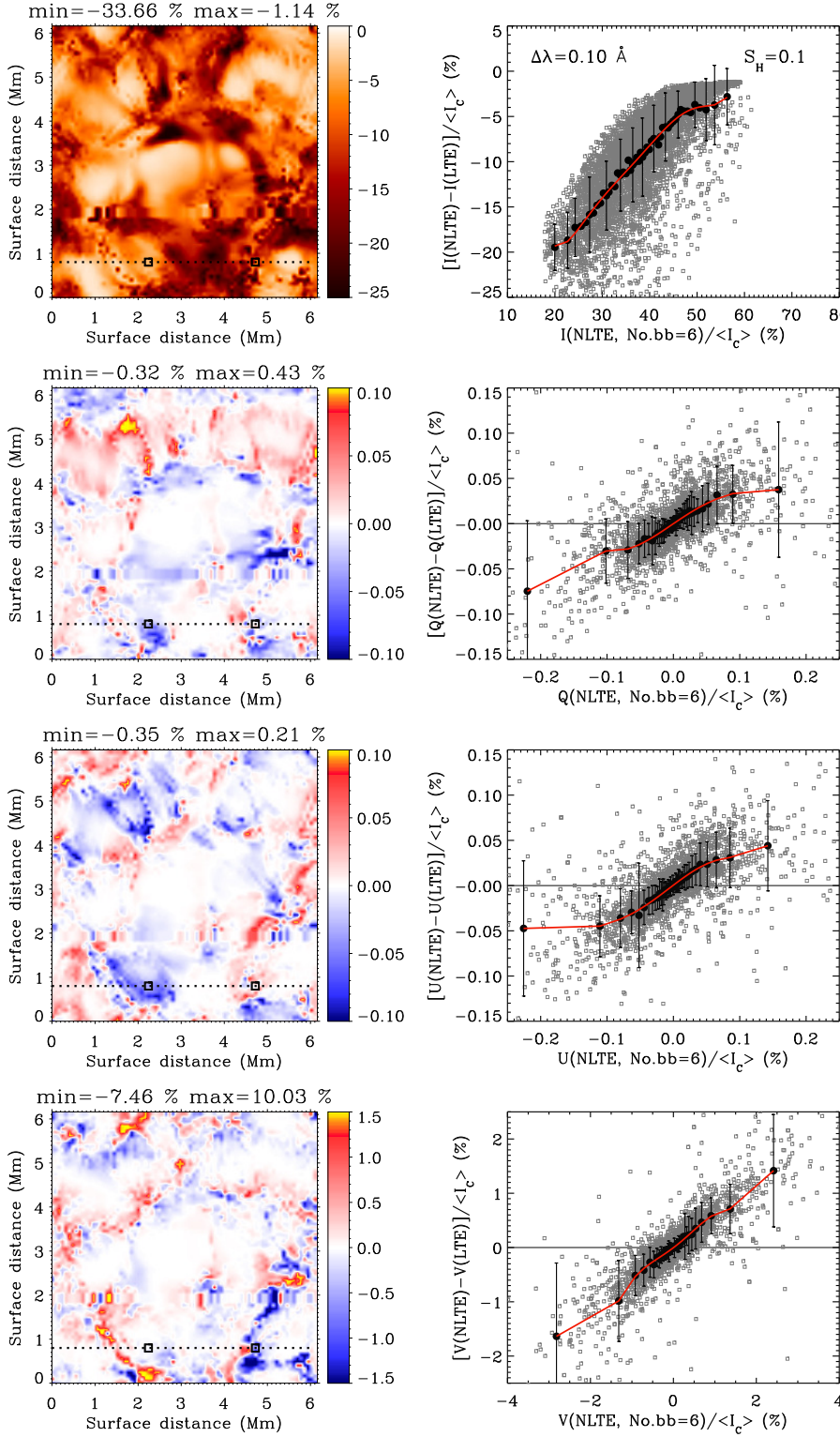


Fig. 11. From top to bottom: changes of the emergent Stokes profiles I , Q , U , and V of the Si I 10 827 Å line at the wavelength $\Delta\lambda = 0.10 \text{ \AA}$ caused by the NLTE effects in the 3D snapshot model. Left: maps of the NLTE changes across surface of the 3D snapshot model. Maximum and minimum values are shown at the top of each map. The horizontal dotted line corresponds to the slice $iy = 10$. The squares mark two surface positions: a granule at $ix = 28$ and an intergranule at $ix = 59$. Right: scatter plots of the NLTE changes. Black circles and vertical lines indicate averages and error bars, correspondingly, over bins with 50 surface points. Red curves represent the sixth-degree polynomial fit to these averages. The NLTE Stokes parameters have been calculated by using the scaling factor $S_H = 0.1$ and the simplest Si I model with six bb transitions (see Fig. 4, bottom right panel). The horizontal thin line indicates a reference point for zero NLTE effects.

the Stokes V signal. Interestingly, this correlation is missing for the Stokes parameters Q and U .

Correlations between the NLTE changes in the Stokes V signals and the magnetic field can be explained as follows. At the formation heights of the Si I 10 827 Å line wings ($-0.25 \leq \Delta\lambda \leq 0.25 \text{ \AA}$), approximately 94% of the 3D model grid-points have magnetic field strength B weaker than 300 G. This means that for the typical values of the model's thermal velocity $\omega_T = 1 \text{ km s}^{-1}$

$$g_{\text{eff}} \frac{\lambda_B}{\lambda_D} < 1,$$

with λ_D the line's Doppler width

$$\lambda_D = \lambda_0 \frac{\omega_T}{c},$$

λ_B the line's Zeeman splitting

$$\lambda_B = 4.67 \times 10^{-13} B(\text{Gauss}) \lambda_0^2 (\text{\AA}),$$

λ_0 the line's wavelength, and c the speed of light. In this case, the Stokes V signal can be estimated using the weak field

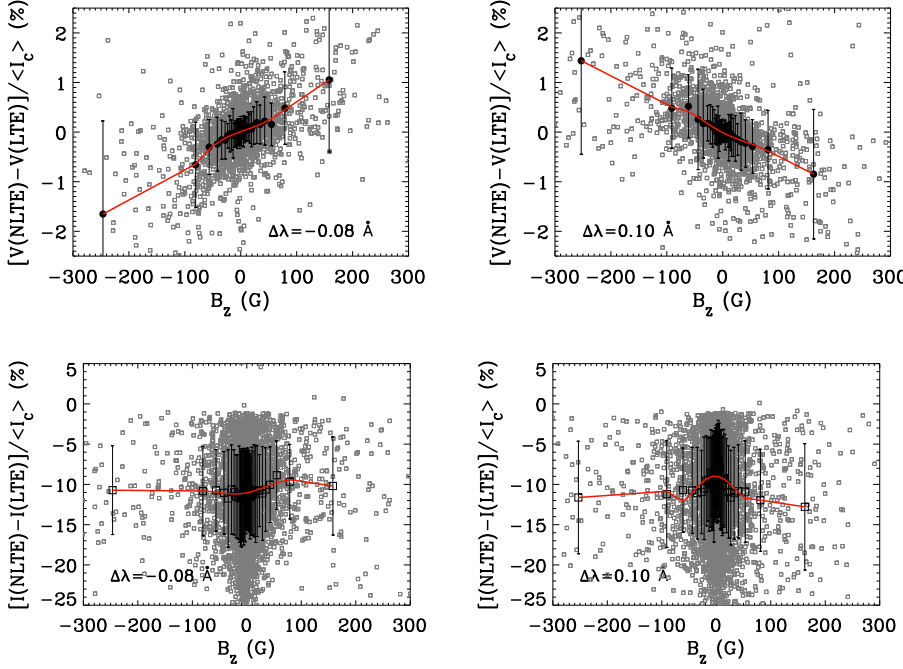


Fig. 12. NLTE changes of the emergent Stokes V profiles in the blue and red wings of the Si I 10827 Å line versus the vertical magnetic field component B_z . *Left:* results for the blue wing at $\Delta\lambda = -0.08 \text{ \AA}$. *Right:* results for the right wing at $\Delta\lambda = 0.10 \text{ \AA}$. The given $\Delta\lambda$ points correspond to the mean wavelength positions of the Stokes V peaks in the blue and red wings of this line (see the top panel of Fig. 3). The B_z values are measured at the heights $H_{\Delta\lambda}(\text{NLTE})$, where the NLTE optical depth at a given wavelength is equal to unity. Black circles and vertical lines indicate averages and error bars, correspondingly, over bins with 50 surface points. The NLTE Stokes parameters are calculated using the simplest Si I model with six bb transitions and assuming $S_H = 0.1$.

Fig. 13. NLTE changes of the emergent Stokes I profiles in the blue and red wings of the Si I 10827 Å line versus the vertical magnetic field component B_z . *Left:* results for the blue wing at $\Delta\lambda = -0.08 \text{ \AA}$. *Right:* results for the right wing at $\Delta\lambda = 0.10 \text{ \AA}$. The NLTE intensity profiles are calculated using the simplest Si I model with six bb transitions and assuming $S_H = 0.1$. For more information, see the caption of Fig. 12.

approximation (see Landi Degl’Innocenti & Landolfi 2004):

$$V = -g_{\text{eff}} \lambda_B \cos \psi \frac{dI}{d\lambda}, \quad (4)$$

where ψ is the angle between the magnetic field and the line-of-sight and $\frac{dI}{d\lambda}$ is the spectral derivative of the intensity. This equation is satisfied when the magnetic field is constant with height. This is a suitable approximation for the wings of the Si I 10827 Å line, which are formed in a rather narrow atmospheric region. The Eq. (4) can be transformed to give the difference between the emergent NLTE and LTE Stokes V profiles

$$\frac{V_{\text{NLTE}} - V_{\text{LTE}}}{\langle I_c \rangle} = -CB_z \frac{d}{d\lambda} \left(\frac{I_{\text{NLTE}} - I_{\text{LTE}}}{\langle I_c \rangle} \right), \quad (5)$$

with $C = 4.67 \times 10^{-13} g_{\text{eff}} \lambda_0^2$. This formula shows that in the weak field approximation the NLTE changes of the emergent Stokes V profiles depend on the product of the vertical component $B_z = B \cos \psi$ of the magnetic field and the spectral derivative $\frac{d}{d\lambda}[(I_{\text{NLTE}} - I_{\text{LTE}})/\langle I_c \rangle]$. As it follows from Fig. 13, in the 3D snapshot model, the NLTE changes $(I_{\text{NLTE}} - I_{\text{LTE}})/\langle I_c \rangle$ of the emergent Stokes profiles I in the blue and red wings of the Si I 10827 Å line are virtually insensitive to B_z . Thus, one can expect that the NLTE changes in the Stokes V amplitudes should mainly respond to one parameter, namely the vertical component of the magnetic field in the line-wing formation region. Figure 12 confirms this conclusion.

Finally, Fig. 14 allows us to estimate to what extent, in general, the NLTE effects shown in Fig. 11 are sensitive to the choice of the silicon model atom. To this end, we derived for all surface (x, y) -grid points of the 3D snapshot model the differences between the NLTE profiles calculated using the simplest Si I model with six bb transitions and the complicated one with 605 bb transitions. In the left panels of Fig. 14 we show the surface maps of

the Stokes profile changes due to using the simplest model atom instead of the complicated one. The right panels of this figure show the scatter of these changes plotted against the NLTE I , Q , U , and V values.

As can be seen from this figure, variations of the Stokes I , Q , U , and V along the surface of the 3D model atmosphere caused by using different model atoms are very small. The scatter plots show only a very weak increase of these changes with increasing Stokes Q , U , and V signals. Comparing the results shown in Figs. 11 and 14, we conclude that the sensitivity of the Stokes profiles of the Si I 10827 Å line to the choice of the silicon model atom is low, although in some surface points the model atom effects are comparable to the NLTE effects. On average, the error caused by using the simplest Si I atomic model is approximately $\pm 1\%$ for the inner wings of the Stokes I profile. For the Stokes Q and U profiles, this error is less than one-hundredth of one percent, while for the Stokes V , this error is larger and can reach a few tenths of a percent. We conclude that our 16-level model atom is suitable for an accurate description of the physics of the Si I 10827 Å line formation.

4. Conclusions

We have carried out NLTE and LTE radiative transfer calculations of the Stokes parameters induced by the Zeeman effect in the diagnostically important Si I 10827 Å line, using a 3D snapshot model of the solar atmosphere taken from a state-of-the-art magneto-convection simulation with small-scale dynamo action (Rempel 2014). This 3D model with zero net magnetic flux taken from the stationary stage of the simulation is characterized by a vertical unsigned flux density $\langle |B_z| \rangle = 80 \text{ G}$ in the model’s visible surface layers. The NLTE calculations were performed using a multilevel radiative transfer code that we developed to compute both NLTE and LTE Stokes I , Q , U , V profiles of the line of

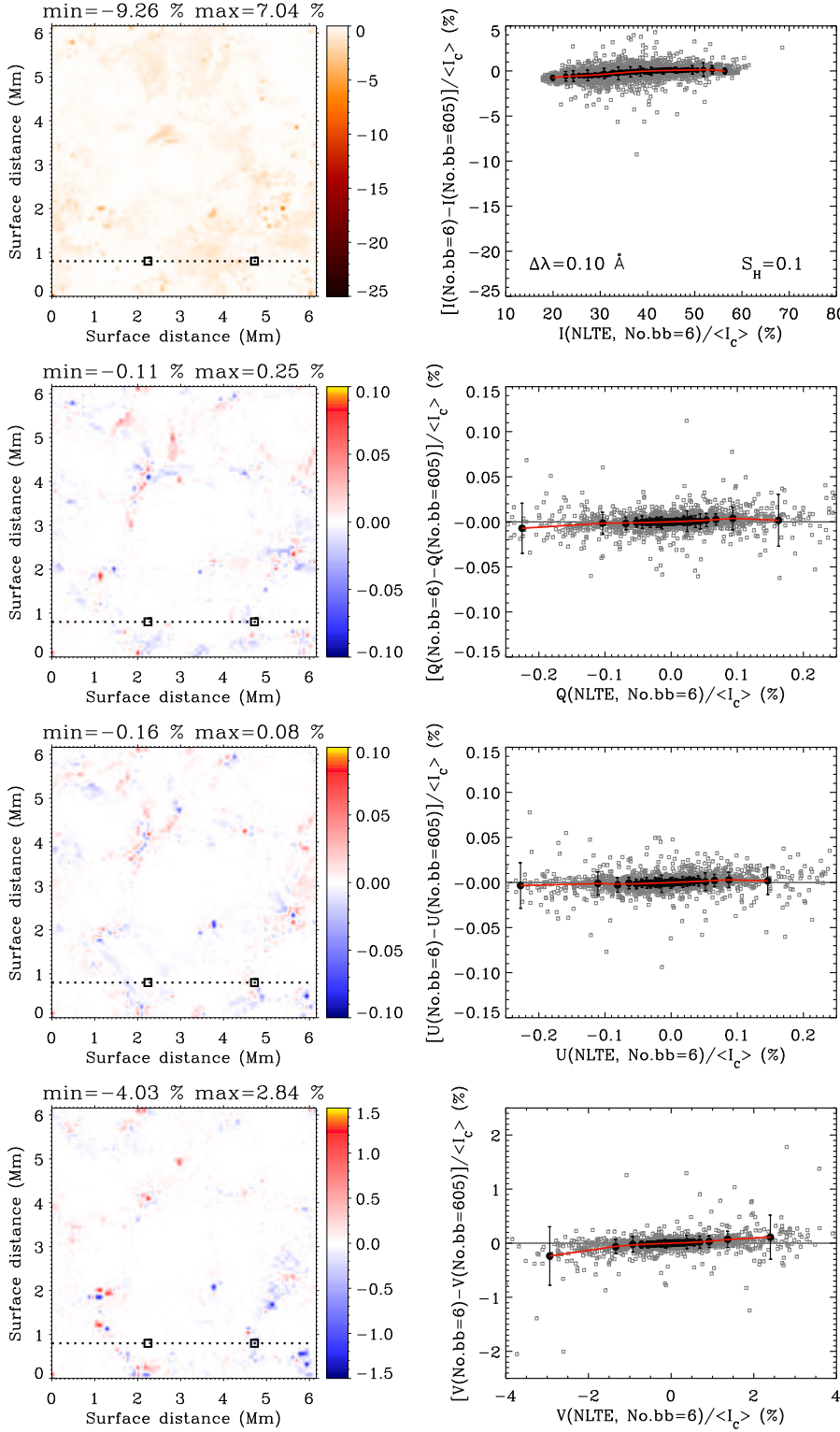


Fig. 14. From top to bottom: changes of the NLTE Stokes profiles I , Q , U , and V of the Si I 10827 Å line at the wavelength point $\Delta\lambda = 0.10 \text{ \AA}$ caused by using different atomic models of Si I. Left: maps of the NLTE changes for the snapshot surface. Maximum and minimum values are shown at the top of each map. Right: scatter plots of the changes. The NLTE Stokes parameters are calculated by using the simplest Si I model with six bb transitions and the complicated model atom with 605 bb transitions (see the bottom left panel of Fig. 4). A horizontal thin line indicate a reference point for zero NLTE effects. For more information, see the caption of Fig. 11.

interest by taking the Zeeman effect into account. We have investigated the sensitivity of the NLTE intensity profiles, as well as of the NLTE linearly and circularly polarized line profiles, to the choice of the silicon model atom. To this end, we constructed several model atoms. Our most comprehensive model atom of Si I + Si II has 296 atomic energy levels connected by 4708 bound-bound and 295 bf radiative transitions. Our simplest model atom has only 16 levels, six bb, and 15 bf radiative transitions.

Our results can be summarized as follows.

An excess of atoms in the lower level of the Si I 10827 Å line, found from the self-consistent solution of the statistical and radiative transfer equations, shifts the formation regions of the line to higher photospheric layers. However, this shift is small. The difference between the NLTE and LTE heights of formation for the Si I 10827 Å line center never exceeds 40 km.

The most important contribution to the source function for the Stokes parameter I of this silicon line comes from terms describing the radiative and collisional coupling of the lower and upper levels of the line with the continuum. The interlocking of

these levels with the rest of the Si I levels is of secondary importance. It produces an insignificant increase in the line source function. In general, the line source function drops below the Planck function in the photosphere at heights above 300 km. The divergence between these two quantities grows rapidly with height in the model atmosphere. As a result, in the formation layers of the Si I 10 827 Å line, the excitation temperature is always lower than the electron temperature. Therefore, LTE diagnostics based on the Si I 10 827 Å line can produce a significant underestimation of the the electron temperature.

The deviations from LTE produce deeper emergent intensity profiles in the Si I 10 827 Å line. The magnitude of this NLTE effect varies considerably across the solar surface. The differences between the NLTE and LTE intensity profiles indicate a well-pronounced dependence on the line depth.

The NLTE impact on the linearly and circularly polarized profiles of the Si I 10 827 Å line is also significant. In the inner wings, around $\Delta\lambda = 0.1$ Å, where most of the Stokes Q , U , and V peaks are located, the profile changes caused by deviation from LTE are comparable to the values of the Stokes amplitudes themselves. These changes increase with the amplitudes of the Stokes profiles. For the Stokes parameter V , there is a clear correlation of the magnitude of the NLTE effects with the magnetic field strength. Such a correlation is not present for the Stokes parameters Q and U .

The changes of the Stokes profiles due to deviations from LTE are significantly larger than the changes caused by using different atomic models. We conclude that the 16-level silicon model atom with six radiative bound-bound transitions is sufficiently accurate for describing the physics of the Si I 10 827 Å line formation, with no significant changes in the emergent Stokes profiles of the line. Generally, in the inner wings of the Stokes I profile, the error, caused by using this simple model atom instead of the complicated model with 210 levels and 605 bb transitions, is approximately $\pm 1\%$. For the Stokes Q and U profiles, the same error is negligibly small and does not exceed 0.01%. The Stokes V profile is more sensitive to the choice of silicon model atom. In particular, this error could reach a few tenths of a percent. However, considering that the Stokes V amplitudes are typically an order of magnitude larger than the Stokes Q and U signals, this errors is also rather small. In conclusion, we recommend using our relatively simple model atom for doing NLTE inversions of the solar Si I 10 827 Å line.

Acknowledgements. We are very grateful to M. Rempel (HAO) for kindly providing the 3D model atmosphere we have used in this investigation. Financial support by the Spanish Ministry of Economy and Competitiveness (MINECO) through projects AYA2014-60476-P and AYA2014-55078-P is gratefully acknowledged. N.G. Shchukina is also grateful to the MINECO, through the 2011 Severo Ochoa Program SEV-2011-0187, which granted her a sabbatical stay at the IAC.

References

- Allen, C. W. 1973, Astrophysical quantities, 3rd edn. (London: Athlone Press)
- Anstee, S. D., & O'Mara, B. J. 1995, *MNRAS*, **276**, 859
- Asensio Ramos, A., Trujillo Bueno, J., & Landi Degl'Innocenti, E. 2008, *ApJ*, **683**, 542
- Asplund, M., Nordlund, Å., Trampedach, R., Allende Prieto, C., & Stein, R. F. 2000, *A&A*, **359**, 729
- Asplund, M., Grevesse, N., Sauval, A. J., & Scott P. 2009, *ARA&A*, **47**, 481
- Bard, S., & Carlsson, M. 2008, *ApJ*, **682**, 1376
- Barklem, P. S., & O'Mara, B. J. 1997, *MNRAS*, **290**, 102
- Barklem, P. S., O'Mara, B.J., & Ross, J. E. 1998, *MNRAS*, **296**, 1057
- Bautista, M. A., Romano, P., & Pradhan, A. K. 1998, *ApJS*, **118**, 259
- Becker, U., Zimmermann, P., & Holweger, H. 1980, *Geochim. Cosmochim. Acta*, **44**, 2145
- Bely, O., & van Regemorter, H. 1970, *ARA&A*, **8**, 329
- Bloomfield, D. Sh., Lagg, A., & Solanki, S. K. 2007, *ApJ*, **671**, 1005
- Borrero, J. M., Bellot Rubio, L. R., Barklem, P. S., & del Toro Iniesta, J. C. 2003, *A&A*, **404**, 749
- Bruls, J. H. M. J., Rutten, R. J., & Shchukina, N. G. 1992, *A&A*, **265**, 237
- Carlsson, M., Rutten, R. J., & Shchukina, N. G. 1992, *A&A*, **253**, 567
- Centeno, R., Collados, M., & Trujillo Bueno, J. 2006, *ApJ*, **640**, 1153
- Centeno, R., Collados, M., & Trujillo Bueno, J. 2009, *ApJ*, **692**, 1211
- Centeno, R., Trujillo Bueno, J., & Asensio Ramos, A. 2010, *ApJ*, **708**, 1579
- Collados, M., López, R., Páez, E., Hernández, E., Reyes, M. et al. 2012, *Astron. Nachr.*, **333**, 872
- Collados, M., Bettonvil, F., Cavaller, L., et al. 2013, in Highlights of Spanish Astrophysics VII, eds. J. C. Guirado, L. M. Lara, V. Quilis, & J. Gorgas, 808
- Cunto, W., Mendoza, C., Ochsenebein, F., & Zeippen, C. J. 1993, *A&A*, **275**, L5
- Denker, C., Lagg, A., Puschmann, K. G., et al. 2012, *IAU Special Session*, **6**, 203
- Drawin, H.W. 1968, *Z. Phys.*, **211**, 404
- Drawin, H.W. 1969, *Z. Phys.*, **225**, 483
- Felipe, T., Khomenko, E., Collados, M., & Beck, C. 2010, *ApJ*, **722**, 131
- Felipe, T., Khomenko, E., Collados, M., & Beck, C. 2011a, *J. Phys.: Conf. Ser.*, **271**, 012040
- Felipe, T., Khomenko, E., & Collados, M. 2011b, *ApJ*, **735**, 65
- Froese-Fischer, C. 2005, *Phys. Rev. A.*, **71**, 042506
- Garz, T. 1973, *A&A*, **26**, 471
- Grevesse, N., & Sauval, A. J. 1998, in Solar Composition and Its Evolution – from Core to Corona, eds. C. Frolich, M. Huber, S. K. Solanki, & R. von Steiger (Dordrecht: Kluwer), 161
- Gurtovenko, E. A., & Kostik, R. I. 1989, Fraunhofer Spectrum and the System of Solar Oscillator Strengths, Russian language (Kiev: Naukova Dumka)
- Holweger, H., & Muller, E. A. 1974, *Solar Phys.*, **39**, 19
- Katsukawa, Y., Watanabe, T., Hara, H., et al. 2012, *IAU Special Session*, 6
- Keil, S. L., Rimmeli, T. R., Wagner, J., Elmore, D., & ATST Team 2011, in Solar Polarization 6, eds. J. R. Kuhn, D. M. Harrington, H. Lin, et al. (San Francisco: ASP), *ASP Conf. Ser.*, **437**, 319
- Khomenko, E. V., Kostik, R. I., & Shchukina, N. G. 2001, *A&A*, **369**, 660
- Khomenko, E. V., Shelyag, S., Solanki, S. K., & Vögler, A. 2005, *A&A*, **442**, 1059
- Kostyk, R. I., & Shchukina, N. G. 2004, *Astron. Rep. (Soviet Astronomy)*, **48**, 769
- Kostyk, R. I., Shchukina, N. G., Khomenko, E. V. 2006, *Astron. Rep. (Soviet Astronomy)*, **50**, 588
- Kuckein, C., Martínez Pillet, V., & Centeno, R. 2012, *A&A*, **542**, A112
- Kuckein, C., Collados, M., & Manso Sainz, R. 2015, *ApJ*, **799**, L25
- Kupka, F., Piskunov, N. E., Ryabchikova, T. A., Stempels, H. C., & Weiss, W. W. 1999, *A&AS*, **128**, 119
- Kurucz, R. L., & Bell, B. 1995, Atomic Line Data (Cambridge, Mass.: Smithsonian Astrophys. Obs.), 23
- Lagg, A. 2007, *Adv. Space Res.*, **39**, 1734
- Landi Degl'Innocenti, E., & Landolfi, M. 2004, Polarization in Spectral Lines (Kluwer Academic Publishers)
- Livingston, W., & Holweger, H. 1982, *ApJ*, **252**, 375
- Maltby, P., Avrett, E. H., Carlsson, M., et al. 1986, *ApJ*, **306**, 284
- Mendoza, C., Eissner, W., LeDourneuf, M., & Zeippen, C. J. 1995, *J. Phys. B.: At. Mol. Phys.*, **28**, 3485
- Mihalas, D. 1978, Stellar Atmospheres, 2nd edn. (San Francisco: Freeman)
- Nahar, S. N., & Pradhan, A. K. 1993, *J. Phys. B.: At. Mol. Phys.*, **26**, 1109
- Neckel, H. 1999, *Solar Phys.*, **184**, 421
- Neckel, H., & Labs, D. 1984, *Solar Phys.*, **90**, 205
- Penn, M. J. 2014, *Liv. Rev. Sol. Phys.*, **11**
- Penn, M. J., & Kuhn, J. R. 1995, *ApJ*, **441**, L51
- Pierce, A. K., & Lopresto, J. C. 1984, *Solar Phys.*, **93**, 155
- Rempel, M. 2014, *ApJ*, **789**, 132
- Ruiz Cobo, B., & del Toro Iniesta, J. C. 1992, *ApJ*, **398**, 375
- Shchukina, N., & Trujillo Bueno, J. 2001, *ApJ*, **550**, 970
- Shchukina, N., & Trujillo Bueno, J. 2011, *ApJ*, **731**, L21
- Shchukina, N., & Trujillo Bueno, J. 2015, *A&A*, **579**, A112
- Shchukina, N., Trujillo Bueno, J., & Asplund, M. 2005, *ApJ*, **618**, 939
- Shchukina, N., Sukhorukov, A., & Trujillo Bueno, J. 2012, *ApJ*, **755**, 176
- Shchukina, N. G., & Trujillo Bueno, J. 2009, in Solar Polarization 5, eds. S. Berdyugina, K. N. Nagendra, & R. Ramelli (San Francisco: ASP), *ASP Conf. Ser.*, **405**, 275
- Shchukina, N. G., Olshevsky, V. L., & Khomenko, E. V. 2009, *A&A*, **506**, 1393
- Shi, J. R., Gehren, T., Butler, K., Mashonkina, L. I., & Zhao, G. 2008, *A&A*, **486**, 303
- Shimizu, T., Tsuneta, S., Hara, H., et al. 2011, in *SPIE Conf. Ser.*, **8148**, 81480B
- Socas-Navarro, H., & Trujillo Bueno, J. 1997, *ApJ*, **490**, 383
- Socas-Navarro, H., de la Cruz Rodríguez, J., Asensio Ramos, A., Trujillo Bueno, J., & Ruiz Cobo, B. 2015, *A&A*, **577**, A7

- Solanki, S., Lagg, A., Woch, J., Krupp, N., & Collados, M. 2003, *Nature*, **425**, 692
- Soltau, D., Volkmer, R., von der Lühe, O., & Berkefeld, T. 2012, *Astron. Nachr.*, **333**, 847
- Stein, R. F. 2012, *Liv. Rev. Sol. Phys.*, **9**, 4
- Sukhorukov, A. V. 2012, *J. Phys. Studies*, **16** (1-2), 1903
- Sukhorukov, A. V., & Shchukina, N. G. 2012, *Kinem. Phys. Celest. Bodies*, **2012**, 28, 169
- Trujillo Bueno, J. 2003, in Stellar Atmosphere Modeling, eds. I. Hubeny, D. Mihalas, & K. Werner, *ASP Conf. Ser.*, **288**, 551
- Trujillo Bueno, J. 2010, in Magnetic Coupling between the Interior and Atmosphere of the Sun, eds. S. S. Hasan, & R. J. Rutten (Berlin: Springer-Verlag), 118
- Trujillo Bueno, J., & Fabiani Bendicho, P. 1995, *ApJ*, **455**, 646
- Trujillo Bueno, J., & Landi Degl'Innocenti, E. 1996, *Sol. Phys.*, **164**, 135
- Trujillo Bueno, J., & Shchukina, N. 2007, *ApJ*, **664**, L135
- Trujillo Bueno, J., Shchukina, N., & Asensio Ramos, A. 2004, *Nature*, **430**, 326
- Unsöld, A. 1955, Physik der Sternatmosphären, 2nd edn. (Berlin: Springer Verlag)
- van Regemorter, H. 1962, *ApJ*, **136**, 906
- Vernazza, J. E., Avrett, E. H., & Loeser, R. 1976, *ApJS*, **30**, 1
- Vernazza, J. E., Avrett, E. H., & Loeser, R. 1981, *ApJS*, **45**, 635
- Vögler, A., & Schüssler, M. 2007, *A&A*, **465**, L43
- Wiegmann, T., Lagg, A., Solanki, S. K., Inhester, B., & Woch, J. 2005, *A&A*, **433**, 701
- Xu, Z., Lagg, A., Solanki, S., & Liu, Y. 2012, *ApJ*, **749**, 138
- Yelles Chaouche, L., Kuckein, C., Martínez Pillet, V., & Moreno-Insertis, F. 2012, *ApJ*, **748**, 23